Research Article
doi.org/10.1002/cmtd.202200033

Chemistry Europe
European Chemical Societies Publishing

Special Collection

In situ X-ray Scattering of the Crystallisation of Basic Magnesium Chlorides using a Laboratory Instrument

Katie S. Pickering,[a] Steven Huband,[b] Kirill L. Shafran,[c] and Richard I. Walton*[a]

We demonstrate a method for in situ monitoring of the crystallisation of basic magnesium chlorides using a laboratory-based SAXS (small angle X-ray scattering)/ WAXS (wide angle X-ray scattering) instrument. By simultaneous acquisition of SAXS/ WAXS, time-resolved particle size and phase evolution information was obtained from room temperature to 120 °C. The WAXS data were analysed using two-phase Rietveld refinements, to produce crystallisation curves. From Avrami-type kinetic analysis two competing mechanistic processes were proposed for the formation of $Mg_3Cl(OH)_5 \cdot 4H_2O$ with a nucleation-type mechanism extending further into the reaction with increased temperature. When comparing SAXS and WAXS, an offset between the consumption of MgO and the reduction of the sphere contribution to the SAXS scattering is observed. This is rationalised by the formation of an amorphous $Mg(OH)_2$ layer on the MgO particle surface. Although laboratory-based SAXS/ WAXS instruments have limitations compared to synchrotron-based sources, we have demonstrated how they can provide new insights into the formation of materials.

Introduction

When synthesising crystalline materials, time-resolved study of their crystallisation is important to understand formation mechanism. This allows for direct observation of reaction kinetics and observation of any intermediate phases to provide mechanistic insight into their formation. With this knowledge, the most efficient reaction conditions for materials preparation can be identified, and potentially these can then be used to control the crystallinity of the material to optimise its properties for practical application. The importance of time-resolved in situ experiments is further emphasised as an alternative to manual quenching of the reaction at various time points, which is time-consuming and can change the nature of the material being analysed, limiting the true mechanistic information that can be determined.[1,2]

In situ powder diffraction experiments have been used to study a variety of crystallisation reactions including solvothermal formation of materials such as the zeotype CoAlPO-5,[3] metal–organic frameworks,[4,5] mixed-metal oxides,[6,7] and the formation of oxides from molten salts.[8] These time-resolved diffraction experiments often rely upon synchrotron-based radiation sources as the high incident X-ray energies and intensities allow penetration of reaction vessels and fast data acquisition, compared to data from laboratory X-ray sources, to yield data with good time resolution. Ideally, in situ diffraction data from which structural information can be determined, such as lattice parameters and crystallite size information from Bragg peak broadening, is required. Complementary to powder XRD, or wide-angle X-ray scattering (WAXS), is the use of small-angle X-ray scattering (SAXS) to monitor the evolution of nanostructure during the formation of materials. For SAXS, synchrotron-based sources allow for fast acquisition times and a wider range of q values, hence lower q values, to be measured therefore giving the opportunity to assess larger length scales. In situ SAXS experiments have been reported using a synchrotron-based source for the formation of a variety of materials, including alumina-zirconia-silicate ceramics,[9] the crystallisation of silicate clays,[10] and have been also used to study growth mechanisms for silica[11] and gold nanoparticles.[12] The use of in situ SAXS using a laboratory-based source has been reported following the formation of silica, gold and silver nanoparticles,[13,14] however, as with diffraction experiments, synchrotron-based SAXS experiments are much more prevalent within literature.

Inherently, SAXS and WAXS provide different information about the system being studied, therefore the combination of these two measurements is important to attain a more holistic view of crystallisation. For example, combined SAXS/WAXS experiments have been used to compare the effect of Zn-doping on hydroxyapatite (HA) nanoparticles,[15] where WAXS data were used to assess the effect of Zn-doping on the crystallinity of the HA nanoparticles, which was then compared to the SAXS signal which was used to assess morphology of the HA nanoparticles. The use of in situ SAXS/WAXS experiments

[a] K. S. Pickering, Prof. R. I. Walton
Department of Chemistry
University of Warwick, CV4 7AL Coventry, (UK)
E-mail: r.i.walton@warwick.ac.uk
[b] Dr. S. Huband
X-Ray Research Technology Platform
Department of Physics
University of Warwick, CV4 7AL Coventry (UK)
[c] Dr. K. L. Shafran
BYK Additives Ltd
Moorfield Road, WA8 3AA Widnes (UK)

Supporting information for this article is available on the WWW under https://doi.org/10.1002/cmtd.202200033

Special Collection
Part of a Special Collection on In Situ and Operando Time-Resolved X-Ray and Neutron Diffraction Studies. Please visit chemistry-methods.org/collections to view all contributions.

Research Article
doi.org/10.1002/cmtd.202200033
Chemistry Europe
European Chemical Societies Publishing

has been reported to study the formation of ZnO nanoparticles in which SAXS was used to evaluate sphere particle size and then compared to the WAXS signal, which was used to evaluate mean particle size using the Scherrer equation.[16] SAXS/WAXS have also been paired with other techniques such as in situ SAXS/WAXS/PDF for the analysis of Ce-stabilised ZrO_2 nanoparticles growth in supercritical fluids,[17] and in situ SAXS/WAXS/UV-Vis to study the growth of Au nanoparticles.[18]

In this paper we demonstrate the use of a laboratory instrument for the measurement of SAXS and WAXS using the example of crystallisation of basic magnesium chloride (BMC) salts. BMC salts are a group of chemical compounds with general formula $Mg_{x+y}(OH)_{2x}Cl_{2y}\cdot z H_2O$, and they are known as a key component within Sorel cement.[19] In recent years, the use of BMC salts as precursor materials for nano-sized $Mg(OH)_2$ have been reported,[20,21] which is of interest due to the flame retardant properties of $Mg(OH)_2$.[22,23] The formation of BMC salts including $Mg_3Cl(OH)_5\cdot 4H_2O$ and $Mg_{10}Cl_2(OH)_{18}\cdot 5H_2O$, was previously studied in situ by Christensen et al. using synchrotron radiation.[24,25] The effect of $MgCl_2$ concentration and reaction temperature were found to be determining factors in which BMC phase was formed and the integrated intensities of selected Bragg peaks were used to determine relative quantities of the phases present. In addition, the FWHM of selected Bragg peaks were used to estimate the particle size of $Mg(OH)_2$ during the reaction. However, the extent to which particle size evolution was studied was limited and no more detailed reports of crystallisation mechanism have been reported in the intervening years. By combination of WAXS and SAXS signals, we aimed to provide mechanistic insight into the crystallisation of BMC salts, in particular $Mg_3Cl(OH)_5\cdot 4H_2O$ and $Mg_5Cl(OH)_9\cdot 2H_2O$, Figure 1, by combining phase identification and quantification from WAXS with particle sizing from SAXS.

Experimental Details

Preparation of MgO

$Mg(OH)_2$ was synthesised via addition of 10 mL of NaOH (1 M) solution to 10 mL of $MgCl_2$ (0.5 M) solution in a 2:1 $[OH^-]$:$[Mg^{2+}]$ molar ratio at a rate of 30 mL/min over a period of 20 min. The resulting precipitate was then left to age for 24 hr in solution then collected using a centrifuge, washed using deionised H_2O and ethanol then dried at 70 °C overnight. The resulting $Mg(OH)_2$ was then calcined at 400 °C for 1 hr then 800 °C for 6 hr resulting in MgO.

Reaction cell design

When designing an in situ reaction cell, two main aspects were considered, the compatibility of the cell with a laboratory based SAXS/WAXS instrument and the ability of the cell to contain the reagent mixture. For the cell to be suitable to be used with the instrument the cell had to be thin, as X-ray scattering data were to be measured in transmission mode and absorption by the reagent mixture needed to be minimised. The sample cell was sealed with Kapton® (polyimide) tape to prevent reagents escaping or dehydration of the cell with heating. With these two considerations in mind a reaction cell consisting of a stainless-steel washer (Ø 4 mm, 0.5 mm thick) sandwiched between two pieces of Kapton® tape was designed, Figure 2.

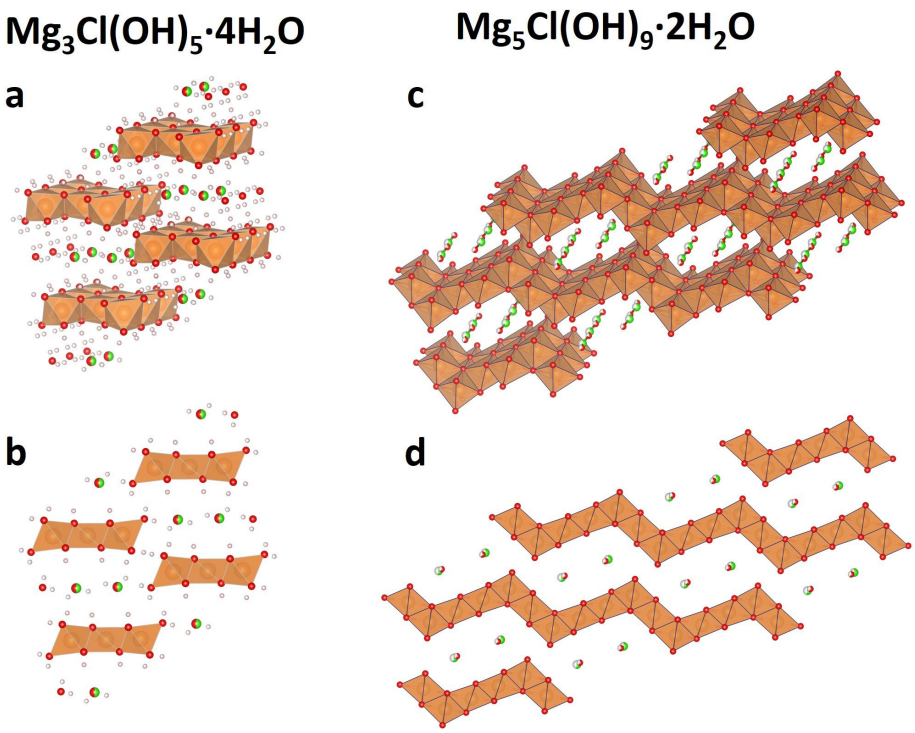

Figure 1. a, b) Views of the crystal structure of $Mg_3Cl(OH)_5\cdot 4H_2O$,[26] and c, d) Views of the crystal structure of $Mg_5Cl(OH)_9\cdot 2H_2O$.[27] In these visualisations the orange octahedra represent Mg, Cl represented by green spheres, O represented by red spheres and H represented by white spheres.

Research Article
doi.org/10.1002/cmtd.202200033
Chemistry Europe
European Chemical Societies Publishing

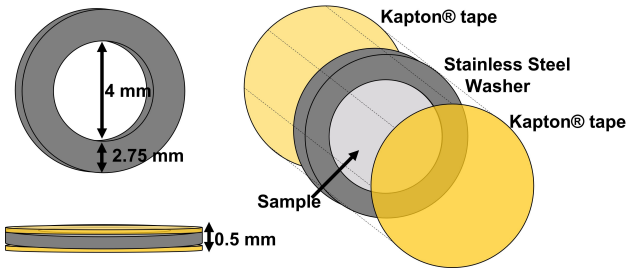

Figure 2. Schematic of reaction cell designed for in situ SAXS/WAXS experiments.

The reaction cell was prepared via addition of 25 μL of $MgCl_2$ (4 M) solution to 0.3 mmol (0.0125 g) of MgO powder with a molar ratio: 3.1:1 $MgCl_2$:MgO i.e. an excess of chloride. The two were mixed and transferred onto the stainless-steel metal washer with Kapton® tape sealing one side of the washer. The other side of the stainless-steel washer was sealed with Kapton® tape ensuring a tight seal so that all reagents remain within the reaction cell.

Measurement of processing of in situ SAXS and WAXS data

SAXS measurements were made using a Xenocs Xeuss 2.0 instrument equipped with a micro-focus $Cu_{K\alpha}$ source collimated with Scatterless slits. The scattering was measured using a Pilatus 300k detector with a pixel size of 0.172 mm × 0.172 mm. The distance between the detector and the sample was calibrated using silver behenate ($AgOOC(CH_2)_{20}CH_3$), giving a value of 2.481(5) m. The magnitude of the scattering vector (q) is given by $q = 4\pi\sin\theta/\lambda$, where 2θ is the angle between the incident and scattered X-rays and λ is the wavelength of the incident X-rays. This gave a q range for the detector of 0.004 $Å^{-1}$ and 0.16 $Å^{-1}$. An azimuthal integration of the 2D scattering profile was performed using FOXTROT[28] software and the resulting 1D data corrected for the absorption, sample thickness and background. Finally, the scattering intensity was then rescaled to absolute intensity using glassy carbon as a standard.[29]

The WAXS data were collected using a Pilatus 100k detector mounted at an angle of 36° from the beam and a distance of 162(2) mm from the sample providing a 2θ range of 18.5–45.5°. An Azimuthal integration of the WAXS data was performed using Xenocs XSACT software.[30]

For variable temperature measurements a Linkam HFSX 350 furnace was used. Once the dwell temperature was reached a set of repeat measurements was made, which consisted of 5 separate 60 s collections followed by a 0.1 s collection with the beam stop removed. The 0.1 data were used for absorption and background corrections on the SAXS data. In this work every 5 WAXS measurement collections were summed. The SAXS signal allowed for a single 60 s data collection to be used for the analysis. The SAXS data were analysed at 30 minute intervals which provided good enough time resolution to follow the changes in the nanostructure.

Kinetic Analysis of WAXS data

A general model for the nucleation and growth of a phase was proposed by Avrami,[31–33] in which the crystallisation of any phase can be explained by a cluster of particles of a stable phase surrounded by an unstable phase. These clusters can be described as nuclei which will continue to grow until reaching a critical size. Above such critical size the nuclei can be described as "growth nuclei" to form the new phase.[33] This model has been refined by various researchers since, and general equation proposed by Erofe'ev, is the simplest to determine a rate constant and to provide some mechanistic insight, Equation (1).[34]

$$\alpha = 1 - \exp\{-(kt)^n\} \quad (1)$$

Here α represents the extent of crystallisation, k is the rate constant of the reaction and n is the Avrami coefficient. A method of analysis was proposed by Sharp and Hancock using the nucleation growth model proposed by Avrami in where plots of $\ln[-\ln(1-\alpha)]$ against $\ln(t)$ should yield a linear function with gradient n and intercept $n\ln(k)$, Equation (2).[35]

$$\ln[-\ln(1-\alpha)] = n\ln(t) + n\ln(k) \quad (2)$$

Avrami-type kinetics were applied to the growth of the product phase, quantified using two-phase Rietveld refinement using the GSAS software[36] with lattice parameters and peak shape parameters refined. The phase fraction of the product phase was taken as the α value to represent the extent of crystallisation.

Fitting of SAXS in situ data

The SAXS signal was fitted using a combination of two models. The first model treated the initial scattering from the MgO as from spherical particles. The intensity from spherical scatterers is given by Equation (3).[37]

$$I(q) = \frac{Scale_{Sphere}}{V}\left[\frac{3V(\sin(qr) - qr\cos(qr))}{(qr)^3}\right]^2 \quad (3)$$

$$I(q) = \mathrm{Scale}_{Porod} * q^{-4} \quad (4)$$

Where $Scale_{Sphere}$ is a scale parameter, V is the volume and r is the radius. The radius is modelled with a log-normal distribution. The second models uses Porod's law and is given by Equation (4), where $Scale_{Porod}$ is a scale factor.[38] The background was fixed at a value of 0.001 for all fits. All modelling was done using the SasView analysis software.[39]

Results and Discussion

Low temperature (28–60 °C) in situ reaction WAXS data

For the reaction carried out at 28 °C the WAXS data initially shows two Bragg peaks at 36.8 and 42.7 2θ which were assigned respectively to the [1 1 1] and [2 0 0] Bragg reflections of MgO.[40] Over a period of 20 hr we observed decay of the Bragg peaks of MgO and growth of diffraction peaks of a new phase, which corresponds to the BMC salt $Mg_3Cl(OH)_5\cdot 4H_2O$,[26] Figure 3a.

The WAXS data were analysed using a two-phase Rietveld refinement, where lattice parameters, micro strain, size and U_{iso} values were refined for both the starting MgO phase and $Mg_3Cl(OH)_5\cdot 4H_2O$ product phase, Table 1. It should be noted that for the Rietveld refinements an instrument parameter file was determined using data measured sample from LaB_6. Figure 4 shows example plots of the Rietveld refinements

Research Article
doi.org/10.1002/cmtd.202200033

Chemistry Europe
European Chemical Societies Publishing

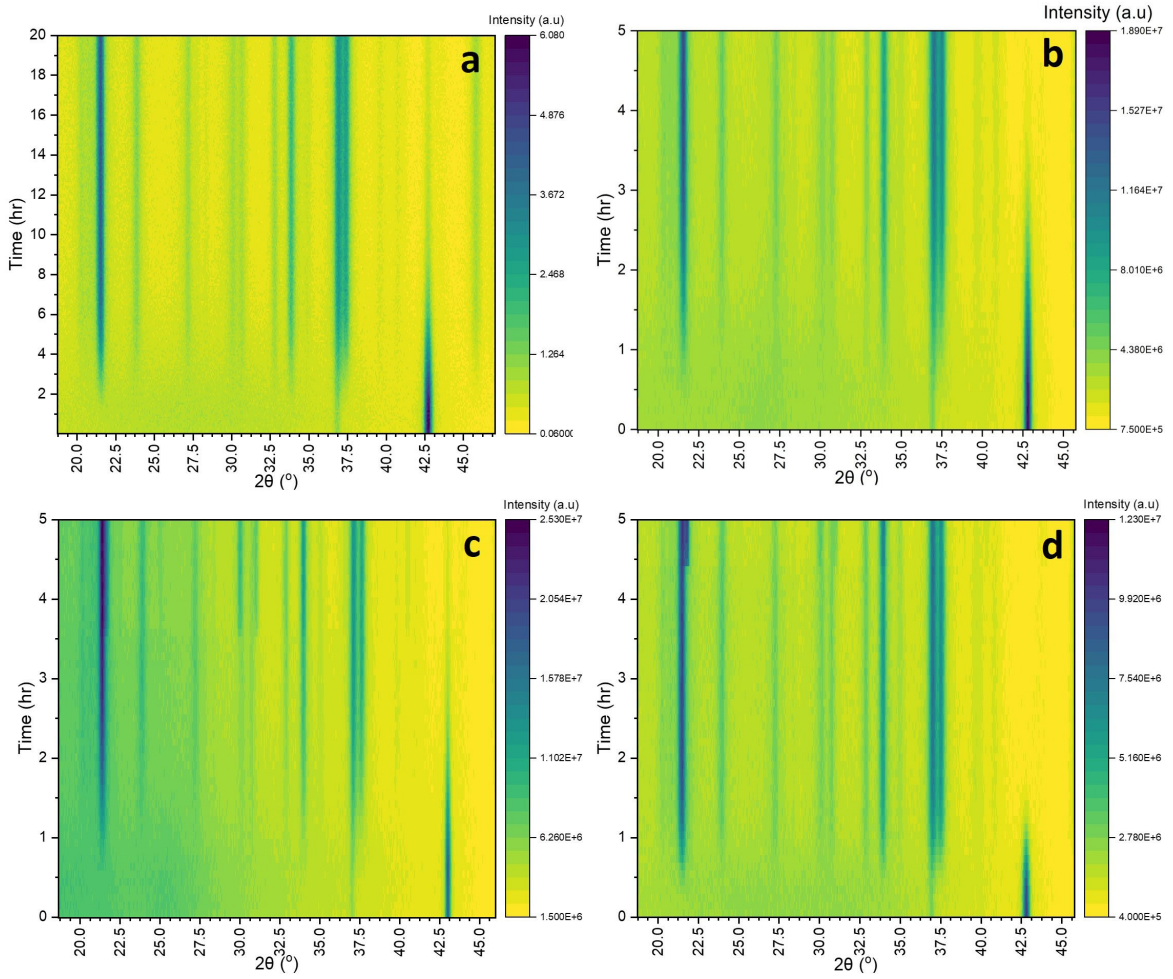

Figure 3. Contour maps of the in situ WAXS data collected at a) 28 °C, b) 40 °C, c) 50 °C and d) 60 °C. All four contour maps show the formation of $Mg_3Cl(OH)_5 \cdot 4H_2O$ from MgO with no crystalline intermediates.

Table 1. A comparison of lattice parameters and cell volume as reported in literature for MgO[30] and $Mg_3Cl(OH)_5 \cdot 4H_2O$,[25] compared to the values obtained from Rietveld refinements using the WAXS data at the beginning and end of the reaction.

Structure	Space Group	Source	*a* [Å]	*b* [Å]	*c* [Å]	β [°]	Cell volume [Å^3]
MgO	$Fm\bar{3}m$	observed	4.2531(8)	–	–	–	76.93(8)
		literature	4.214(1)	–	–	–	74.83(7)
$Mg_3Cl(OH)_5 \cdot 4H_2O$	$P2/m$	observed	9.7380(1)	3.1701(7)	8.3789(2)	113.86(3)	236.55(4)
		literature	9.6412(5)	3.1506(2)	8.3035(5)	113.98(6)	230.44(7)

carried out for the starting MgO material, at 3 hr and of the product at 20 hr. It should be noted that any small discrepancy between the peak intensities from the refinement compared to the observed data could be attributed to preferred orientation within the sample. Considering the refined lattice parameter values for the product $Mg_3Cl(OH)_5 \cdot 4H_2O$ in Table 1, we observe all lattice parameters to be slightly larger than the literature values, and this is most evident along the *a* axis, with the refined value being approximately 0.09 Å larger than in the literature.

Using the refined values of structural parameters, Table 1, the phase fraction of the two phases were refined for all intermediate times, so that a crystallisation curve for the weight fractions of MgO and $Mg_3Cl(OH)_5 \cdot 4H_2O$ could be plotted. We observe 50% consumption of the MgO starting material and the formation of 50% of the $Mg_3Cl(OH)_5 \cdot 4H_2O$ product at 2.5 hr ($t_{0.5}$), then at 8 hr we observe 95% consumption of MgO with $>99\%$ consumption of reagents being observed at 20 hr, Figure 4d.

The same reaction was then conducted at 40, 50 and 60 °C and $Mg_3Cl(OH)_5 \cdot 4H_2O$ was found to be the resultant product at all three temperatures, Figure 3. All three temperatures all show a similar evolution, with the consumption of the MgO phase and the crystallisation of the $Mg_3Cl(OH)_5 \cdot 4H_2O$ phase with no diffraction peaks from crystalline intermediates observed. After sequential Rietveld refinement of the in situ data at 40, 50,

Research Article
doi.org/10.1002/cmtd.202200033
Chemistry Europe
European Chemical Societies Publishing

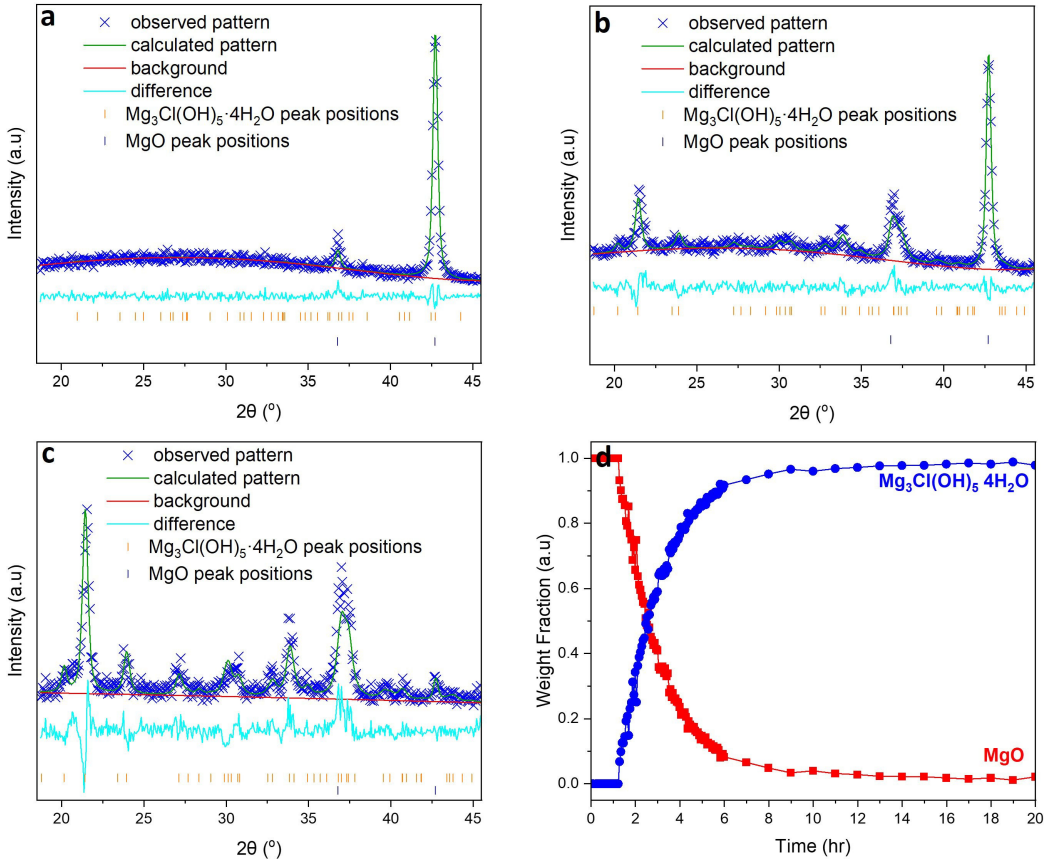

Figure 4. Two-phase Rietveld refinement of MgO and $Mg_3Cl(OH)_5 \cdot 4H_2O$ at 28 °C using the WAXS data measured at a) 0 hr, b) 3 hr, c) 20 hr, d) crystallisation curve of $Mg_3Cl(OH)_5 \cdot 4H_2O$ from MgO, weight fraction of each phase was evaluated using a two phase Rietveld refinement.

60 °C, $t_{0.5}$ was evaluated to be 0.88, 0.79 and 0.49 hr, respectively.

Considering the crystallisation curves produced from Rietveld refinements, Avrami-type kinetics were used to quantify the kinetics of product formation. When this was applied to the in situ data we observe for all four temperatures two distinct linear regions with different gradients hence different *n* values, Figure 5. It should be noted that lower values of α were not included in the calculations as they would be subjected to larger error with respect to resolution of the peaks within the background.

At 28 °C, the first linear region can be fitted for $\alpha < 0.57$ with n = 2.14 and the second region applies for $\alpha \geq 0.57$ and yields a gradient of n = 1.40. As the reaction temperature is increased the first region extends further into the crystallisation period. In the first stage of the reaction, we see Avrami coefficients (*n*) between 2.06–2.42 whereas in the second stage of the reaction we observe Avrami coefficients between 1.20–1.40, Table 2. The change in Avrami coefficient observed is distinct enough between the two regions to suggest competition between two mechanistic processes and a switch of dominant crystallisation mechanism part way through the crystallisation.

As discussed above the Avrami coefficient (*n*) gives mechanistic insight into the reaction. Typically Avrami coefficient of $n \approx 0.5$ indicates a diffusion controlled mechanism,

Table 2. The α ranges analysed using a Sharp–Hancock plot and the calculated Avrami coefficients and rate constants for the reaction at 28, 40, 50 and 60 °C.

Temperature [°C]	Extent of reaction [α]	Avrami coefficient [*n*]	Rate constant [k/s^{-1}]
28	$0.36 < \alpha < 0.57$	2.14 ± 0.12	$9.17 \times 10^{-5} \pm 6.81 \times 10^{-5}$
	$0.57 \leq \alpha < 0.91$	1.40 ± 0.02	$8.94 \times 10^{-5} \pm 1.91 \times 10^{-5}$
40	$0.03 < \alpha < 0.60$	2.44 ± 0.10	$2.82 \times 10^{-4} \pm 1.31 \times 10^{-4}$
	$0.60 \leq \alpha < 0.99$	1.24 ± 0.01	$2.61 \times 10^{-4} \pm 2.98 \times 10^{-5}$
50	$0.35 < \alpha < 0.79$	2.06 ± 0.06	$2.94 \times 10^{-4} \pm 1.02 \times 10^{-4}$
	$0.79 \leq \alpha < 0.95$	1.20 ± 0.03	$3.32 \times 10^{-4} \pm 9.32 \times 10^{-5}$
60	$0.25 < \alpha < 0.82$	2.42 ± 0.02	$4.86 \times 10^{-4} \pm 4.73 \times 10^{-5}$
	$0.82 \leq \alpha < 0.99$	1.30 ± 0.03	$5.88 \times 10^{-4} \pm 1.57 \times 10^{-4}$

Research Article
doi.org/10.1002/cmtd.202200033
Chemistry Europe
European Chemical Societies Publishing

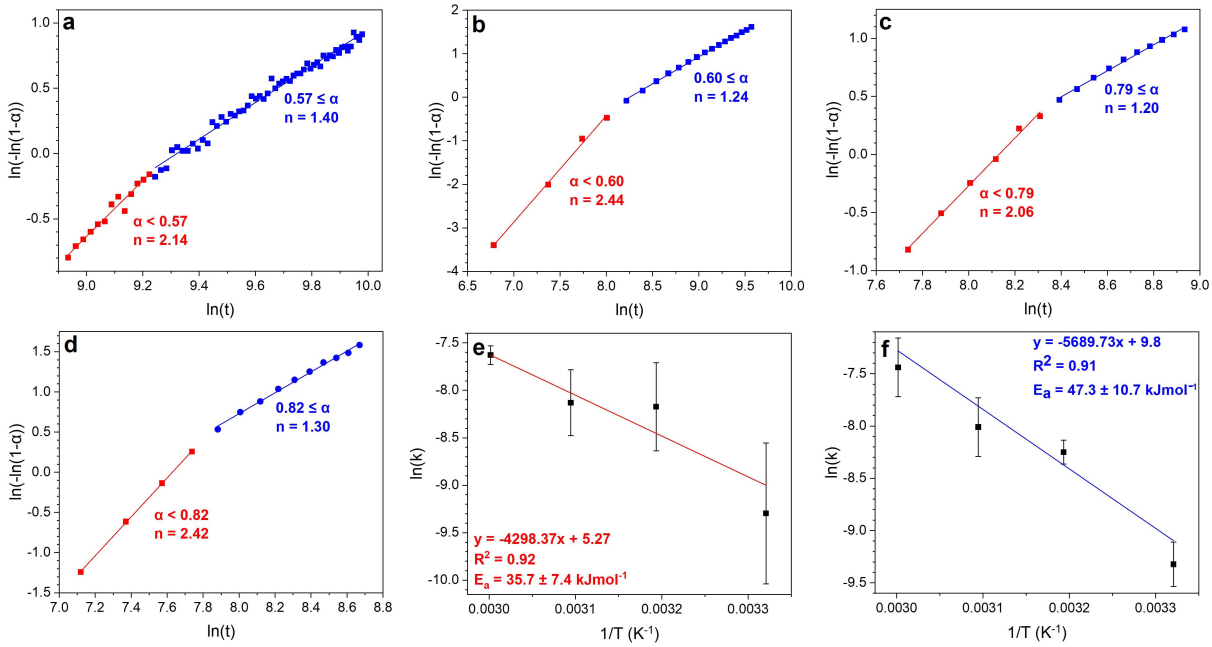

Figure 5. Sharp-Hancock plots for the formation of $Mg_3Cl(OH)_5 \cdot 4H_2O$ at a) 28 °C, b) 40 °C, c) 50 °C and d) 60 °C. e) Arrhenius plot of the formation of $Mg_3Cl(OH)_5 \cdot 4H_2O$ using k values as evaluated using the first region observed in the Sharp-Hancock plots and f) Arrhenius plot using k values as evaluated using the second region observed in the Sharp-Hancock plots.

$n \approx 1$a phase-boundary controlled mechanism and $n = 2$–3 nucleation controlled mechanism.[35,41] We observe two Avrami coefficients of $n = 2.06$–2.42 for the first stage of the reaction suggesting dependence on the nucleation of the particles and a coefficient between $n = 1.20$–1.40 suggesting dependence on the transport of the reagents, Table 2.

With increasing temperature we observe the first region extending over a wider α range, suggesting that the nucleation step extends further into the crystallisation of the BMC phase with increasing temperature. This is mirrored with the second region representing the transport of reagents, spanning across a decreasing range of α values with increasing temperature. For both the nucleation and the transport limited region we observe temperature dependence on the calculated rate constant. An Arrhenius plot was then made for each region. Considering the linear region for the first stage of the reaction the activation energy was calculated to be 35.7 kJ mol^{-1}. However, if we consider the rate constants from the second stage of the reaction, the activation energy is calculated to be higher than that of the nucleation stage of the reaction with a value of 47.3 kJ mol^{-1}.

If one relates this to the interplay between the two regions observed in the Avrami fitting, we can suggest that with increasing temperature nucleation (first region) extends further into the reaction as this requires a lower activation energy (35.7 kJ mol^{-1}). The second (transport) region becomes less prominent within the reaction, which is evident by the higher calculated activation energy (47.3 kJ mol^{-1}). Therefore, at higher temperatures nucleation dominates until all nucleation sites are created at which point transport becomes significant within the reaction.

We consider it is reasonable to propose two different mechanistic processes occurring with different activation energies, as similar situations have been presented in literature for the crystallisation of various different materials. Avrami kinetics have been applied to the intercalation of $LiNO_3$ into $Al(OH)_3$, and a change in Avrami coefficient at $\alpha \approx 0.5$, indicated a shift in reaction mechanism from diffusion controlled to nucleation controlled.[42] A shift in reaction mechanism with temperature has also been reported in literature for the hydrothermal crystallisation of $BaTiO_3$ it was found that at 100 °C the Sharp–Hancock plot displayed two linear regions ($n = 0.2$ and $n = 1.7$), whereas at higher temperature (150 °C) only one linear region was observed ($n = 3.7$).[43] Similarly in the study of aqueous recrystallisation of Mg^{2+}/Al^{3+} double layered hydroxides, using Sharp–Hancock plots at 25 °C one linear region was observed whereas at 60 °C two linear regions were observed, then at higher temperatures (120 °C) the first stage of the reaction became less dominant.[44] In a study of formation of TiO_2 nanoparticles, Eltzholtz et al. fitted Sharp–Hancock plots using two linear regions.[45] The first region was concluded to be nucleation type mechanism and the second a phase boundary type mechanism, as determined using the Avrami coefficients. Considering these examples in the literature, it is reasonable that there are two distinct mechanistic processes in the formation of $Mg_3Cl(OH)_5 \cdot 4H_2O$, and that the extent to which nucleation-type mechanism extents into the reaction is dependent on temperature.

Research Article
doi.org/10.1002/cmtd.202200033
Chemistry Europe
European Chemical Societies Publishing

Low temperature (28–60 °C) in situ SAXS data

The initial MgO starting material was analysed using SAXS, and from the scattering curve we observe a plateau at low q (Å^{-1}) values with an elbow like feature around 0.01 q (Å^{-1}), which confirmed the presence of nano-sized material. The data were fitted using a sphere mode and the sphere diameter was evaluated to be 27.65 ± 0.02 nm, Figure 6a.

Figure 6d shows the in situ SAXS scattering curves for the reaction at 28 °C where over time we detect a reduction in intensity from the elbow feature at 0.01 q (Å^{-1}) and the emergence of a linear slope. It is noteworthy that a change in position of the elbow at 0.01 q (Å^{-1}) is not seen, but instead a reduction of intensity of the feature over time. If the feature had changed position (i.e. moved to different q values) it would suggest a reduction in size of the particles. However, what we observe is a reduction of intensity: this could be explained by either a reduction in the number of nanoparticles or a reduction in the scattering length density difference between the particle and the matrix/solvent. As the reaction proceeds, the linear slope in the SAXS signal starts to dominate, until this is the main feature observed. We suggest that this linear slope can be interpreted as the presence of material >160 nm, which could be particles or related to an aggregate formed during the reaction. As the reaction proceeds the proportion of the reaction mixture that contains material of this size increases hence the intensity of the linear slope increases over time.

The SAXS scattering response during the reactions can be split into three stages. In the initial stage the scattering from the initial MgO particles can modelled as a log-normal distribution of spheres. As the reaction progresses there is an intermediate stage where both model are required to fit the scattering. In the final stage the scattering is fully modelled using Porod's law. Two examples of a combined fit to the scattering at 5 hr and 20 hr are shown in Figure 6b and Figure 6c with the scattering from spheres shown by the red line, the Porod scattering by the blue line and the combined fit by the green line.

As we used a combined sphere and Porod gradient model, we can assess the extent to which each the model contributes to the scattering observed. The scale factor for both the sphere model and Porod model were both normalised and the assumption that the scale of each model correlated to the volume fraction of that type of material within the reaction cell was made.

Considering the SAXS fitted data we observe an initial sphere diameter of 27.65 nm. We then observe a minor reduction in the fitted sphere diameter over time, (26.50 nm at 2 hr, 22.12 nm at 4 hr). This suggests that the scale factors for the spherical model and Porod slope will provide more insight into the reaction process than the change in size of the initial nanomaterial.

When comparing the weight fraction MgO (from Rietveld analysis of the WAXS) over time with the sphere scale from the SAXS fitting, we observe a delay in the reduction of the sphere

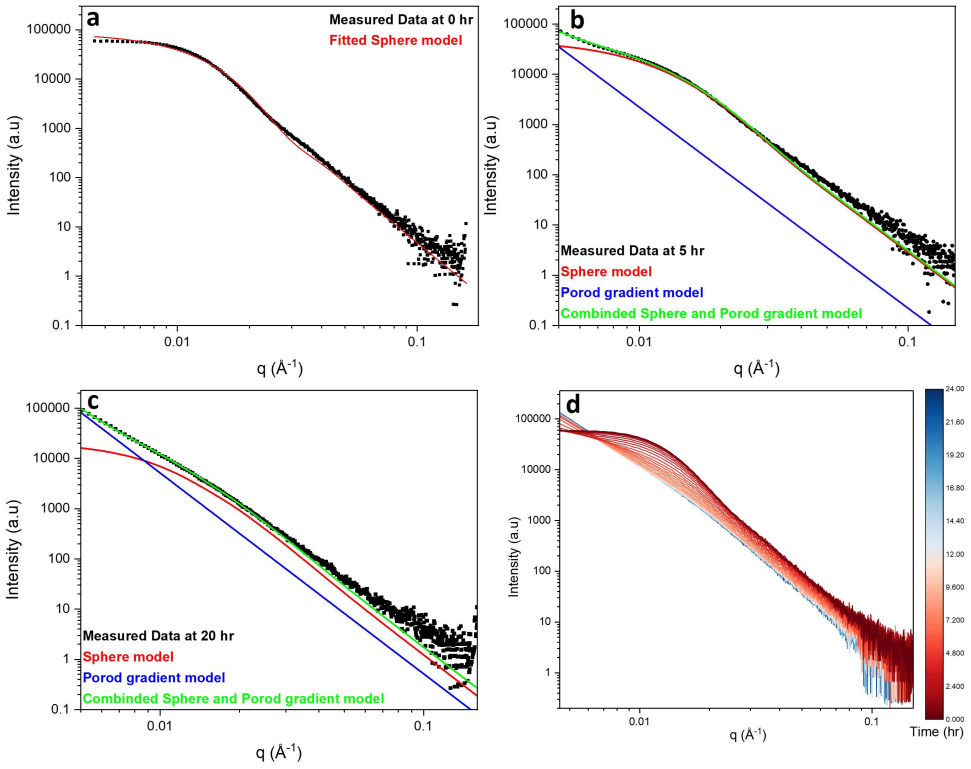

Figure 6. a) SAXS fitted data of the MgO starting material, data fitted using a sphere model, b) SAXS in situ data for the formation of $Mg_3Cl(OH)_5 \cdot 4H_2O$ at 28 °C collected at 5 hr modelled using a combined sphere and Porod gradient model, c) SAXS in situ data collected at 20 hr and d) Full set of SAXS in situ measurements taken at 28 °C.

Research Article
doi.org/10.1002/cmtd.202200033
Chemistry Europe
European Chemical Societies Publishing

scale compared to the decay of the MgO phase in the WAXS, Figure 7a. We propose that an initial reaction with the solution occurs on the surface of the particle, forming an amorphous $Mg(OH)_2$ layer. This results in a reduction in the MgO WAXS signal but does not cause a change in the nanoparticle size. The formation of an amorphous $Mg(OH)_2$ layer would allow for Mg^{2+} to be released into the solution, allowing for the product to start forming before we observe reduction in the contribution of spheres in the SAXS signal. It is important to note that the sphere model was used to represent the MgO starting material, however from the SAXS signal we cannot distinguish between different phases. Therefore, when analysing the spherical contribution to the SAXS scattering it is possible we are not only looking at the reagent material but also possibly looking at the formation of sphere-like product which may also contribute the sphere scattering.

If we consider the Porod model contribution to the SAXS scattering, we also observe an offset in the WAXS signal of the product forming and the onset of the Porod gradient. This suggests that the product starts to crystallise and then larger material is observed in the SAXS signal. We propose that this is due the product forming which then agglomerates together to form material that can no longer be characterised via SAXS, Figure 7b.

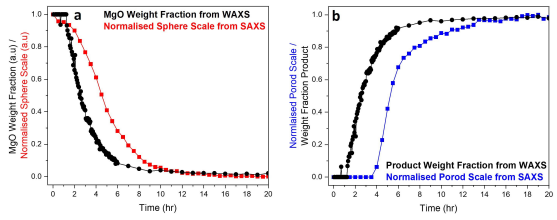

Figure 7. a) Comparison of MgO weight fraction, as evaluated from two phase Rietveld refinement of the WAXS data with respect to time, and the normalised sphere contribution to the SAXS fitted model. b) Comparison of the $Mg_3Cl(OH)_5 \cdot 4H_2O$ weight fraction and the Porod gradient contribution to the SAXS fitted model with respect to time.

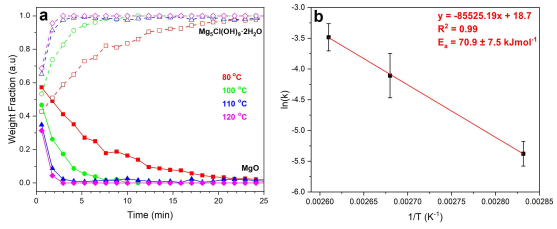

Figure 8. a) Crystallisation curve for the formation of $Mg_5Cl(OH)_9 \cdot 2H_2O$ from MgO, produced via two phase Rietveld refinement of the in situ WAXS data at varied temperature (80, 100 110 and 120 °C) and b) Arrhenius plot for the formation of $Mg_5Cl(OH)_9 \cdot 2H_2O$ from MgO at 80, 100 and 110 °C.

High temperature (80–120 °C) in situ SAXS/WAXS experiments

High temperature in situ reactions between 80–120 °C were carried out. In each case no crystalline intermediates were observed, Supporting Information, Figure S1, as with the lower temperature reactions, but here the product formed was identified to be $Mg_5Cl(OH)_9 \cdot 2H_2O$.[27] This is consistent with results reported in literature that at higher temperature, under the same conditions, the BMC salt phase formed would have a higher hydroxide content.[24] It is noteworthy that the formation of $Mg_5Cl(OH)_9 \cdot 2H_2O$ occurs directly with no evidence for the formation of $Mg_3Cl(OH)_5 \cdot 4H_2O$ as a transient phase.

Similarly to the method used for the low temperature reactions, crystallisation curves were produced via two-phase Rietveld refinement of the WAXS diffraction data, Figure 8a and Supporting Information, Figure S2. The refined parameters of the BMC phase $Mg_5Cl(OH)_9 \cdot 2H_2O$ are shown in Table 3. Overall the refined lattice parameters result in a cell volume of 568.408 Å^3, which is larger than reported literature value of 562.862 Å^3.[27] This can be rationalised by the fact that the observed WAXS data were measured at 120 °C whereas the reported literature values were measured at 20 °C.

It is to be expected that with increasing temperature the rate of reaction will significantly increase, this being the most evident at 120 °C with the reaction reaching completion within 3 mins. With the reaction proceeding at this rate, kinetic information could only be obtained for temperatures lower than 120 °C. Using an Arrhenius plot the activation energy for the crystallisation of $Mg_5Cl(OH)_9 \cdot 2H_2O$ was calculated to be 70.9 kJ mol^{-1}, Figure 8b.

The increased rate of the reaction is further emphasised in the SAXS in situ data. Figure 9 shows the in situ SAXS scattering curves for the reaction at 120 °C, where within minutes we observe a linear slope in the SAXS data. The presence of the linear region indicates larger material that cannot be quantified using the laboratory based SAXS/WAXS instrument due to the observable q range. In this case, using a laboratory based SAXS/WAXS instrument we are sensitive to particles <160 nm, to quantify material larger than this q values below 0.004 Å^{-1} would need to be measured, hence a synchrotron-based source would be required in order to quantify the size of the material observed here.

Conclusions

We have demonstrated the use of a laboratory based SAXS/WAXS instrument to follow the formation and crystallisation of two BMC salt phases in situ. The in situ WAXS data were

Table 3. A comparison of lattice parameters and cell volume for $Mg_5Cl(OH)_9 \cdot 2H_2O$ as reported in literature[26] compared to the values obtained from a Rietveld refinement of the product at 120 °C.

Structure	Source	Space Group	*a* [Å]	*b* [Å]	*c* [Å]	β [°]	Cell volume [Å^3]
$Mg_5Cl(OH)_9 \cdot 2H_2O$	observed	*I*2/*m*	22.1479(2)	3.1628(2)	8.1830(9)	97.43(3)	568.40(8)
	literature		22.2831(6)	3.1350(1)	8.1315(7)	97.75(3)	562.86(2)

analysed using a two-phase Rietveld refinement, from which Avrami-type kinetics was inferred. Sharp–Hancock plots were produced, from which two distinct linear regions were observed. The two linear regions were attributed to two mechanistic processes present in the formation of $Mg_3Cl(OH)_5 \cdot 4H_2O$, nucleation and transport. With variable temperature experiments we observed the nucleation-type mechanism extend further into the reaction with increased temperature, suggesting at higher temperatures nucleation dominates until all nucleation sites are created at which point transport becomes significant within the reaction. This was attributed to the nucleation-type mechanism having a lower calculated activation energy of 35.7 kJ mol^{-1} as compared to the transport-type mechanism which has a calculated activation energy of 47.3 kJ mol^{-1}.

The in situ SAXS data were analysed using a combined sphere model and Porod gradient with a fixed value of −4. The sphere contribution to the model was used to represent the MgO starting material, and the Porod slope was used to model the presence of larger material in the system. When comparing the SAXS and WAXS signals an offset was observed between the decay of the MgO phase in the WAXS and the reduction in the sphere contribution in the SAXS scatting. This discrepancy was rationalised by the presence of an amorphous $Mg(OH)_2$ layer on the MgO particle surface.

High temperature reactions (80–120 °C) were also followed in situ and the formation of $Mg_5Cl(OH)_9 \cdot 2H_2O$ was observed. The activation energy for the crystallisation of $Mg_5Cl(OH)_9 \cdot 2H_2O$ was calculated to be 70.9 kJ mol^{-1}. The rate of reaction significantly increases with increasing temperature, as a result we observe rapidly the formation of material too large to quantify using laboratory based SAXS instrument. Previous in situ studies of BMC salt formation using synchrotron based radiation relied only upon integrated intensities of Bragg reflections to determine relative quantities of each phase, from which an activation energy was calculated using the Arrhenius expression.[23,24] In this work we have taken analysis further by executing full pattern fitting to the in situ data using two-phase Rietveld refinement. By analysis using Avrami-type kinetics we have gained insight into the formation mechanism for $Mg_3Cl(OH)_5 \cdot 4H_2O$ and how we suggest this varies with temperature. In Christensen's earlier work, the extent to which particle size was analysed was limited to observation of the FWHM for the one Bragg reflection for the formation of $Mg(OH)_2$ at varied temperatures, and that only showed a weak trend for slight particle growth.[24] In this work, by use of a SAXS detector we were able to monitor particle size evolution in more detail than previously reported.

In conclusion, we have demonstrated that although synchrotron-based sources do have significant advantages especially with respect to the size of particles observable using SAXS, in situ data can be collected using a laboratory-based instruments to allow observation of crystallisation of materials and determination of quantitative kinetic information. Further mechanistic detail concerning the formation of basic magnesium chlorides is needed to build a more complete model for crystallisation and in future work we will investigate the use of complementary spectroscopic methods to examine local atomic arrangement, for example to examine the formation of disordered hydroxide layers as intermediates.

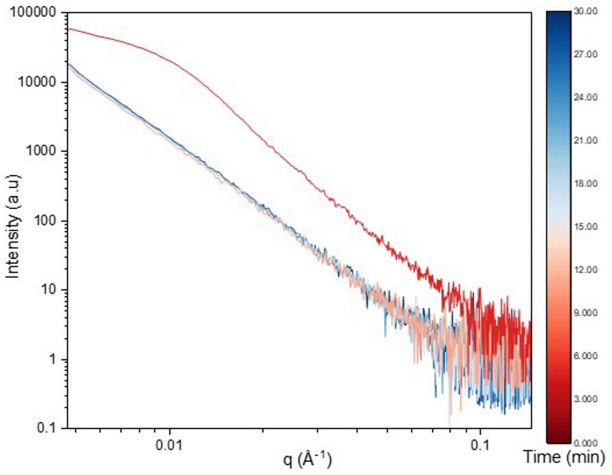

Figure 9. SAXS in situ data for the formation of $Mg_5Cl(OH)_9 \cdot 2H_2O$ at 120 °C.

Acknowledgements

We would like to thank University of Warwick Analytical-Science Centre of Doctoral Training (AS-CDT) and BYK Additives Ltd for funding this project. We also thank the University of Warwick's X-ray Research Technology Platform for provision of the instrumentation used in this research.

Conflict of Interest

The authors declare no conflict of interest.

Data Availability Statement

The research data underpinning this article can be accessed at: http://wrap.warwick.ac.uk/167451

Keywords: basic magnesium chloride · crystallisation · in situ · SAXS/WAXS · X-ray diffraction

[1] N. Pienack, W. Bensch, *Angew. Chem. Int. Ed.* **2011**, *50*, 2014–2034; *Angew. Chem.* **2011**, *123*, 2062–2083.
[2] K. M. Ø. Jensen, C. Tyrsted, M. Bremholm, B. B. Iversen, *ChemSusChem* **2014**, *7*, 1594–1611.
[3] K. Simmance, G. Sankar, R. G. Bell, C. Prestipino, W. Van Beek, *Phys. Chem. Chem. Phys.* **2010**, *12*, 559–562.
[4] Y. Wu, M. I. Breeze, G. J. Clarkson, F. Millange, D. O'Hare, R. I. Walton, *Angew. Chem. Int. Ed.* **2016**, *55*, 4992–4996; *Angew. Chem.* **2016**, *128*, 5076–5080.
[5] H. H. M. Yeung, Y. Wu, S. Henke, A. K. Cheetham, D. O'Hare, R. I. Walton, *Angew. Chem. Int. Ed.* **2016**, *55*, 2012–2016; *Angew. Chem.* **2016**, *128*, 2052–2056.

[6] G. Philippot, E. D. Boejesen, C. Elissalde, M. Maglione, C. Aymonier, B. B. Iversen, *Chem. Mater.* **2016**, *28*, 3391–3400.
[7] S. L. Skjærvø, G. K. Ong, O. G. Grendal, K. H. Wells, W. Van Beek, K. Ohara, D. J. Milliron, S. Tominaka, T. Grande, M. A. Einarsrud, *Inorg. Chem.* **2021**, *60*, 7632–7640.
[8] S. J. Moorhouse, Y. Wu, H. C. Buckley, D. O'Hare, *Chem. Commun.* **2016**, *52*, 13865–13868.
[9] D. Le Messurier, R. Winter, C. M. Martin, *J. Appl. Crystallogr.* **2006**, *39*, 589–594.
[10] K. A. Carrado, L. Xu, S. Seifert, D. Gregory, K. Song, R. E. Botto, *Chem. Mater.* **2000**, *12*, 320–322.
[11] D. J. Tobler, S. Shaw, L. G. Benning, *Geochim. Cosmochim. Acta* **2009**, *73*, 5377–5393.
[12] J. Polte, T. T. Ahner, F. Delissen, S. Sokolov, F. Emmerling, A. F. Thünemann, R. Kraehnert, *J. Am. Chem. Soc.* **2010**, *132*, 1296–1301.
[13] A. Schwamberger, B. De Roo, D. Jacob, L. Dillemans, L. Bruegemann, J. W. Seo, J. P. Locquet, *Nucl. Instrum. Methods Phys. Res. Sect. B* **2015**, *343*, 116–122.
[14] P. R. A. F. Garcia, O. Prymak, V. Grasmik, K. Pappert, W. Wlysses, L. Otubo, M. Epple, C. L. P. Oliveira, *Nanoscale Adv.* **2020**, *2*, 225–238.
[15] H. Maleki-Ghaleh, M. H. Siadati, Y. Omidi, M. Kavanlouei, J. Barar, A. Akbari-Fakhrabadi, K. Adibkia, Y. Beygi-Khosrowshahi, *Mater. Chem. Phys.* **2022**, *276*, 1–12..
[16] M. Herbst, E. Hofmann, S. Förster, *Langmuir* **2019**, *35*, 11702–11709.
[17] J. Becker, M. Bremholm, C. Tyrsted, B. Pauw, K. M. O. Jensen, J. Eltzholt, M. Christensen, B. B. Iversen, *J. Appl. Crystallogr.* **2010**, *43*, 729–736.
[18] X. Chen, J. Schröder, S. Hauschild, S. Rosenfeldt, M. Dulle, S. Förster, *Langmuir* **2015**, *31*, 11678–11691.
[19] S. A. Walling, J. L. Provis, *Chem. Rev.* **2016**, *116*, 4170–4204.
[20] W. Fan, S. Sun, L. You, G. Cao, X. Song, *J. Mater. Chem.* **2003**, *13*, 3062–3065.
[21] W. Fan, S. Sun, X. Song, W. Zhang, H. Yu, X. Tan, G. Cao, *J. Solid State Chem.* **2004**, *177*, 2329–2338.
[22] D. Jin, X. Gu, X. Yu, G. Ding, H. Zhu, K. Yao, *Mater. Chem. Phys.* **2008**, *112*, 962–965.
[23] S. Mishra, S. H. Sonawane, R. P. Singh, A. Bendale, K. Patil, *J. Appl. Polym. Sci.* **2004**, *94*, 116–122.
[24] A. N. Christensen, P. Norby, J. C. Hanson, *Acta Chem. Scand.* **1995**, *49*, 331–334.
[25] A. N. Christensen, P. Norby, J. C. Hanson, *J. Solid State Chem.* **1995**, *114*, 556–559.
[26] K. Sugimoto, R. E. Dinnebier, T. Schlecht, *Acta Crystallogr. Sect. B* **2007**, *63*, 805–811.
[27] R. E. Dinnebier, D. Freyer, S. Bette, M. Oestreich, *Inorg. Chem.* **2010**, *49*, 9770–9776.
[28] G. Viguier, R. Girardot, FOXTROT Version 3.3.4 Academic Edition, SAXS 2D data reduction, Xenocs/SOLEIL Synchrotron, **2021**.
[29] F. Zhang, J. Ilavsky, G. G. Long, J. P. G. Quintana, A. J. Allen, P. R. Jemian, *Metall. Mater. Trans. A* **2010**, *41*, 1151–1158.
[30] Xenocs, XSACT: X-ray Scattering Analysis and Calculation Tool Version 2.4, SAXS & WAXS data analysis software, Xenocs, **2021**.
[31] M. Avrami, *J. Chem. Phys.* **1939**, *7*, 1103–1112.
[32] M. Avrami, *J. Chem. Phys.* **1940**, *8*, 212–224.
[33] M. Avrami, *J. Chem. Phys.* **1941**, *9*, 177–184.
[34] B. Erofe'ev, *Dokl. Acad. Sci. URSS* **1946**, *52*, 511–514.
[35] J. D. Hancock, J. H. Sharp, *J. Am. Ceram. Soc.* **1972**, *55*, 74–77.
[36] B. H. Toby, R. B. Von Dreele, *J. Appl. Crystallogr.* **2013**, *46*, 544–549..
[37] A. Guinier, G. Foutnet, *Small-Angle Scattering of X-Rays*, John Wiley & Sons, Inc., New York, **1955**.
[38] G. Porod, *Kolloid-Z.* **1951**, *124*, 83–114.
[39] M. Doucet, J. H. Cho, G. Alina, Z. Attala, J. Bakker, W. Bouwman, P. Butler, K. Campbell, T. Cooper-Benun, C. Durniak et al., SASView Version 5.0.4, SAXS analysis software, Zenodo, 2021, DOI: 10.5281/zenodo.4467703.
[40] V. G. Tsirelson, A. S. Avilov, Y. A. Abramov, E. L. Belokoneva, R. Kitaneh, D. Feil, *Acta Crystallogr. Sect. B* **1998**, *54*, 8–17.
[41] L. Sharp, G. Brindley, B. N. Achr, *J. Am. Ceram. Soc.* **1966**, *49*, 379–382
[42] G. R. Williams, D. O'Hare, *J. Phys. Chem. B* **2006**, *110*, 10619–10629.
[43] M. Özen, M. Mertens, F. Snijkers, P. Cool, *Ceram. Int.* **2016**, *42*, 10967–10975.
[44] F. Millange, R. I. Walton, D. O'Hare, *J. Mater. Chem.* **2000**, *10*, 1713–1720.
[45] J. R. Eltzholtz, C. Tyrsted, K. M. Ø. Jensen, M. Bremholm, M. Christensen, J. Becker-Christensen, B. B. Iversen, *Nanoscale* **2013**, *5*, 2372–2378.

Manuscript received: April 29, 2022
Version of record online: August 9, 2022